

Article

Density Functional Theory Study of Oxygen Evolution Reaction Mechanism on Rare Earth Sc-Doped Graphene

Yiwen Liu ¹, Mengqi Liao ¹, Yuting Hu ¹, Tae-Gwan Lee ², Ravindranadh Koutavarapu ^{3,*} ,
Shaik Gouse Peera ^{2,*}  and Chao Liu ^{1,*} ¹ Faculty of Materials Metallurgy and Chemistry, Jiangxi University of Science and Technology, Ganzhou 341000, China² Department of Environmental Science and Engineering, Keimyung University, Daegu 42601, Republic of Korea³ Department of Robotics Engineering, College of Mechanical and IT Engineering, Yeungnam University, Gyeongsan 38541, Republic of Korea

* Correspondence: ravindra_physicist@ynu.ac.kr (R.K.); gouse@kmu.ac.kr (S.G.P.); liuchao198967@126.com (C.L.)

Abstract: The development of a stable catalyst with excellent catalytic performance for the oxygen evolution reaction (OER) in alkaline environments is a key reaction in various electrochemical technologies. In this work, single-atom catalysts (SACs) systems in which scandium (Sc), a rare earth metal, with different N/C coordination environments ($\text{ScN}_x\text{C}_{3-x}\text{@SACs}$ and $\text{ScN}_x\text{C}_{4-x}\text{@SACs}$ of Sc) were systematically studied with the help of density functional theory (DFT) calculations. The results of the structural thermodynamic stability analysis indicated that the $\text{ScN}_x\text{C}_{3-x}\text{@SACs}$ and $\text{ScN}_x\text{C}_{4-x}\text{@SACs}$ systems are more stable with increasing N atom doping concentration around Sc. The ScN_3 , ScN_3C , and ScN_4 with better stability were selected as the objects of subsequent research. However, ScN_3 and ScN_4 form $\text{Sc}(\text{OH})_2\text{N}_3$ and $\text{Sc}(\text{OH})_2\text{N}_4$ structures with double-hydroxyl groups as ligands because of the strong adsorption of OH species, whereas the strong adsorption of OH species by ScN_3C causes structural instability. Here, the overpotential (η) of $\text{Sc}(\text{OH})_2\text{N}_3$ was 1.03 V; $\text{Sc}(\text{OH})_2\text{N}_4$ had two reaction paths and the η of path 1 was 0.80 V, which was 0.30 V lower than that of path 2. Therefore, $\text{Sc}(\text{OH})_2\text{N}_4$ can be used as a stable and promising OER catalyst with easy desorption of O_2 and good cycle performance. The hydroxyl ligand modification of $\text{ScN}_x\text{C}_{3-x}\text{@SACs}$ and $\text{ScN}_x\text{C}_{4-x}\text{@SACs}$ provides a method for studying the catalytic performance of other rare earth elements.

Keywords: oxygen evolution reaction (OER); N/C coordination; hydroxyl ligands; DFT calculation

Citation: Liu, Y.; Liao, M.; Hu, Y.; Lee, T.-G.; Koutavarapu, R.; Peera, S.G.; Liu, C. Density Functional Theory Study of Oxygen Evolution Reaction Mechanism on Rare Earth Sc-Doped Graphene. *Batteries* **2023**, *9*, 175. <https://doi.org/10.3390/batteries9030175>

Academic Editors: Sylvain Franger, Carolina Rosero-Navarro and Sang Bok Lee

Received: 30 December 2022

Revised: 10 March 2023

Accepted: 15 March 2023

Published: 17 March 2023



Copyright: © 2023 by the authors. Licensee MDPI, Basel, Switzerland. This article is an open access article distributed under the terms and conditions of the Creative Commons Attribution (CC BY) license (<https://creativecommons.org/licenses/by/4.0/>).

1. Introduction

The current society is confronted with the challenge of increasing energy demand and the associated environmental problems caused by energy consumption. As a result, the global research community has prioritized the search for pollution-free, sustainable, and efficient energy production/energy conversion technologies [1–3]. In this regard, the development of rechargeable fuel cells and metal–air battery technologies has been perceived as a promising clean and sustainable energy technology because of its high energy conversion efficiency and power density [4,5]. In these energy conversion technologies, the anodic half-cell reaction, i.e., oxygen evolution reaction (OER), plays a vital role in the efficiency of regenerative fuel cells and metal–air battery technologies [6–8]. Due to the instability of transition-metal-based materials in acidic circumstances, electrocatalytic OER is typically carried out in alkaline conditions [9]. Nonetheless, the OER is often deemed the main obstacle in rechargeable fuel cell and metal–air battery technologies because of the slow and sluggish kinetics of this four-electron transfer reaction, which restricts the high efficiency of these energy conversions [10,11].

Extensive research and a wide range of engineered catalysts have been proposed in an effort to increase OER kinetics [12–15]. Among them, RuO_2 and IrO_2 have exhibited excellent OER catalytic activities [16,17]. However, both are unstable during the reaction process and are oxidized to form RuO_4 and IrO_3 , respectively, which preferentially dissolve in solution [18]. Furthermore, Ru and Ir are precious metals with scarce resources and high costs, making them unsuitable for large-scale, commercial applications [19]. Thus, it is essential to develop excellent alternative electrocatalysts for OER with better stability and to explore affordable OER electrocatalysts with good catalytic activity.

On the other hand, carbon-based catalysts, such as graphene, have advantages such as a large specific surface area, high acid/alkaline stability, and excellent electronic conductivity [20,21]. In recent years, carbon-based catalysts have become the focus of OER research. However, pure graphene is catalytically inert [20,22]. Heteroatom doping, especially N doping of graphene, is found to be the most effective method to improve the intrinsic activity of the catalyst because of the variation in the spin density and charge of the carbon atom next to the doped N atom, together with high specific surface area, excellent conductivity, and outstanding electrochemical properties [23–26]. Single-atom catalysts (SACs), in which a central single metal atom surrounded by different doping atoms forms coordination and disperses in the supporting material, have gained special interest for various catalytic reactions because of their excellent stability, maximum utilization of the metallic electrochemically active surface area, strong metal–support interactions, and unique properties [27–29]. Metal–organic frameworks (MOFs) have proven to be a promising approach for SAC preparation. Carbonization of MOFs can result in N-doped carbon materials with N/C coordination, which provides an abundance of anchor points for the fixation of a single metal atom, resulting in SAC stability [30,31]. Accordingly, the synthesis of single transition metal–nitrogen moiety-supported carbon catalysts (M–N–C, M = Fe/Co, etc.) as OER catalysts has been extensively investigated, and these are the most widely studied SACs [32,33]. Unfortunately, the instability of Fe–N–C SACs limits their further application owing to the high Fenton catalytic activity of Fe [34]. On the other hand, the OER overpotential in the Co–N–Gra system is 0.69 V. In addition, due to cobalt’s toxicity, poisoning can happen during the manufacturing and recycling processes, and cobalt leakage also results in battery damage [35].

Rare earth (RE) elements, such as Sc, Nd, Gd, and Ce, have attracted increasing attention in the field of electrocatalytic applications because of their unique multi-electron properties and electronic structure, high electrical conductivity, good stability, abundant reserves, and excellent electrocatalytic activity [36–42]. In particular, Sc atoms have the characteristics of a small atomic radius, suitability for single/double atom vacancy doping, and multi-electron properties [43–45]. Moreover, it has been well established that SACs with a Sc atom as the active site of the catalytic center have a good catalytic effect on CO oxidation and the reduction of CO_2 and N_2 [46–48]. Sc@SACs are synthesized on a carbon support with high yields in the literature. Catalytic activities are observed in Sc_1/NC SACs despite the fact that Sc-based nanomaterials are typically inert to room temperature electrochemical processes. This is because N and C coordination alters the local electronic structure of Sc single atoms. The catalytic properties of rare earth single atoms not only showcase the miraculous impact of SACs, but also advocate for the use of rare earth catalysts in electrochemical reactions that take place at room temperature [46–48]. Therefore, Sc@SACs systems with varied N/C coordinations as OER catalysts for increased OER kinetics are worth investigating. However, there has been little research on the use of Sc for OER applications. As a result, we investigated the effect of Sc and its coordination environment on the OER in alkaline media.

In this work, Sc@SACs systems with different N/C coordination ratios ($4\text{ScN}_x\text{C}_{3-x}$ @SACs and $7\text{ScN}_x\text{C}_{4-x}$ @SACs) were studied in detail by performing density functional theory (DFT) calculations. Based on the calculation of the thermodynamic formation energy, the influence of N/C coordination on $\text{ScN}_x\text{C}_{3-x}$ @SACs and $\text{ScN}_x\text{C}_{4-x}$ @SACs was studied. Thermodynamic stability screening indicated that the formation energies of the ScN_3 , ScN_3C , and ScN_4 structures

were negative, making them more stable than other structures. Further, simulation analysis in an alkaline environment found that ScN_3 and ScN_4 can exist as $\text{Sc}(\text{OH})_2\text{N}_3$ and $\text{Sc}(\text{OH})_2\text{N}_4$, respectively, because of the strong adsorption of OH species. However, the $\text{Sc}(\text{OH})_2\text{N}_3\text{C}$ structure formed by ScN_3C was unstable. The catalytic reactions of $\text{Sc}(\text{OH})_2\text{N}_3$ and $\text{Sc}(\text{OH})_2\text{N}_4$ structures with double-hydroxyl ligand modification for the OER under alkaline conditions were also studied. Finally, the influence of N atom doping concentration, also known as different N/C coordination and hydroxyl ligand effects, on the catalytic performance of the structure was described.

2. Computational Details

2.1. Methods

Dmol³ [49] is the algorithm used for any calculations involving density functional theory with no restrictions on spin. Electronic exchange and correlation effects were described using the generalized gradient approximation [50] with the Perdew–Burke–Ernzerhof functional. After taking into account the ion–electron interaction in the DFT semi-core pseudopotentials [51] and the double numerical plus polarization [52] basis sets, we proceeded to the core treatment. Grimme’s [53] method was used to calculate the dispersion’s share. Energy convergence tolerances were 1×10^{-5} Ha, maximum force tolerances were 0.002 Ha Å⁻¹, and displacement tolerances were 0.005 Å. To hasten the convergence, an orbital occupancy smear of 0.005 Ha was used. The calculations used a cutoff radius for global orbits in actual space that was of fine quality. Electronic structure calculations were performed on a $15 \times 15 \times 1$ k-point grid, whereas geometry optimization and energy calculations were performed on a $5 \times 5 \times 1$ k-point grid in the Brillouin zone. For this exercise, we assumed that water has a dielectric constant of 78.54 and utilized the conductor-like screening model [54] to mimic this environment.

2.2. Models

To begin, a $5 \times 5 \times 1$ periodic graphene supercell was built and separated by a 30 Å vacuum layer to eliminate periodic interactions. By substituting a Sc atom for either one or two carbon atoms, $\text{ScN}_x\text{C}_{3-x}$ @SACs and $\text{ScN}_x\text{C}_{4-x}$ @SACs were created. In place of the C atoms around the central Sc atom, the extremely electronegative N atoms acted as anchors. There were four structures with three coordinations ($\text{Sc-N}_x\text{C}_{3-x}$ @SACs) and seven structures with four coordinations ($\text{Sc-N}_x\text{C}_{4-x}$ @SACs). Three distinct architectures of ScN_2C_2 are depicted in Figure 1. $\text{ScN}_2\text{C}_2\text{-h}$ is a hexa-atomic ring composed of two nitrogen atoms, two carbon atoms, and a Sc metal atom, whereas $\text{ScN}_2\text{C}_2\text{-p}$ is a penta-atomic ring composed of two nitrogen atoms, two carbon atoms, and a Sc metal atom. The two N atoms in $\text{ScN}_2\text{C}_2\text{-o}$ are situated on either side of the Sc atom.

2.3. Computational Contents

(1) Formation energy (ΔE_f)

The ΔE_f of different $\text{ScN}_x\text{C}_{3-x}$ @SACs and $\text{ScN}_x\text{C}_{4-x}$ @SACs structures can be calculated as follows:

$$\Delta E_f = E_{\text{Sc-N}_x\text{C}_{3-x}} + (x + 1)\mu_C - E_{\text{Graphene}} - \mu_{\text{Sc}} - x\mu_N, \quad x = 0, 1, 2, 3 \quad (1)$$

$$\Delta E_f = E_{\text{Sc-N}_x\text{C}_{4-x}} + (x + 2)\mu_C - E_{\text{Graphene}} - \mu_{\text{Sc}} - x\mu_N, \quad x = 0, 1, 2, 3, 4 \quad (2)$$

where $E_{\text{Sc-N}_x\text{C}_{3-x}}$ and $E_{\text{Sc-N}_x\text{C}_{4-x}}$ are the total energies of the optimized structures of $\text{ScN}_x\text{C}_{3-x}$ @SACs and $\text{ScN}_x\text{C}_{4-x}$ @SACs, respectively. E_{Graphene} represents the total energy of a single layer of a $5 \times 5 \times 1$ graphene supercell. μ_C , μ_{Sc} , and μ_N are the chemical potentials of C, Sc, and N atoms, respectively. μ_C is equal to the energy of each carbon atom in the $5 \times 5 \times 1$ graphene supercell, μ_N is the half energy of the isolation N_2 molecule, and μ_{Sc} is the energy of one Sc atom, which can be obtained from the total energy of the Sc unit cell divided by the number of atoms. $x + 1$, $x + 2$ and x are the numbers of C atoms discharged from the original graphene and doped N atoms, respectively.

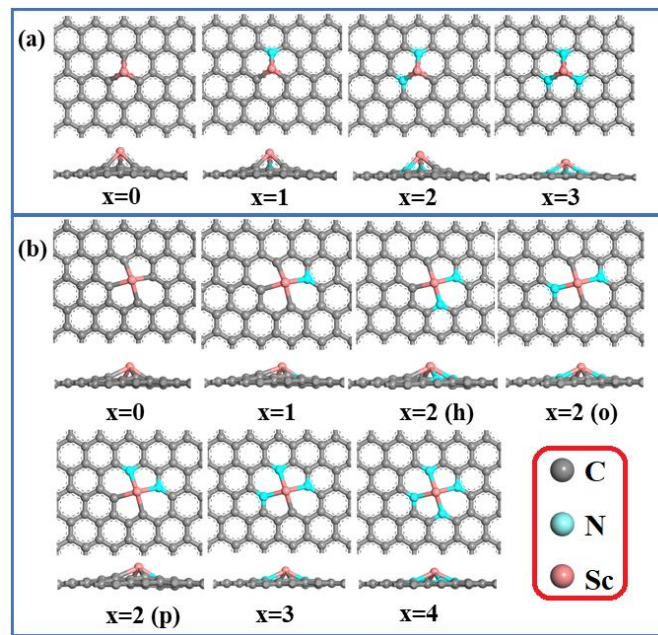


Figure 1. Optimized geometries of the (a) $\text{Sc-N}_x\text{C}_{3-x}\text{@SACs}$ and (b) $\text{Sc-N}_x\text{C}_{4-x}\text{@SACs}$ structures.

(2) Adsorption energy (ΔE_{ads})

The ΔE_{ads} of intermediates can be calculated as follows:

$$\Delta E_{ads} = E_{*n} - E_* - E_n \quad (3)$$

where E_{*n} , E_* , and E_n are the total energies of the $\text{ScN}_x\text{C}_{3-x}\text{@SACs}/\text{ScN}_x\text{C}_{4-x}\text{@SACs}$ with n adsorbed species, the $\text{ScN}_x\text{C}_{3-x}\text{@SACs}$ and $\text{ScN}_x\text{C}_{4-x}\text{@SACs}$, and the isolated n species, respectively.

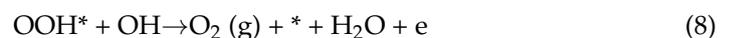
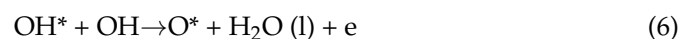
(3) Gibbs free energy variation (ΔG)

The ΔG of each reaction step can be calculated as follows [55]:

$$\Delta G = \Delta E + \Delta ZPE - T\Delta S + \Delta G_U + \Delta G_{pH} \quad (4)$$

where ΔE , ΔZPE , and ΔS represent the variation in the reaction energy, zero-point energy (ZPE), and entropy, respectively. T is 298.15 K, which represents the room temperature. $\Delta G_U = -neU$, where n is the number of electron transfers during these elementary reactions, U is the electrode potential, and ΔG_U is the free energy contribution related to the applied electrode potential U . $\Delta G_{pH} = K_B T \times \ln 10 \times pH$, where K_B is the Boltzmann constant, and the value of pH is 14 in an alkaline environment.

(4) Reaction steps of the OER in an alkaline environment



* represents the adsorption sites on the catalyst surface. *OOH, *O, and *OH are the oxygen-containing intermediate products of the OER process. g and l represent the gas and liquid phases, respectively.

The overpotential of the OER is defined as follows (η^{OER}):

$$\eta^{\text{OER}} = [\Delta G_1, \Delta G_2, \Delta G_3, \Delta G_4]_{\max} / e - 0.402 \text{ V} \quad (9)$$

3. Results and Discussion

3.1. Stability of Sc and N Co-Doped Graphene

First, the constructed structures ($\text{ScN}_x\text{C}_{3-x}\text{@SACs}$ and $\text{ScN}_x\text{C}_{4-x}\text{@SACs}$) were optimized to obtain the formation energies (ΔE_f) of different Sc and N co-doped graphene structures, which can be used to analyze the influence of the N atom doping concentration and different coordination environments on structural stability. The formation energies of the different structures are shown in Figure 2, and the detailed values are listed in Table S1. The results showed that the structures of ScN_3 , ScN_3C , and ScN_4 were more stable than the other structures because of the negative value of the formation energy. In general, lower ΔE_f values indicate higher structural stability. Furthermore, with the increase in the N atom doping concentration, the ΔE_f values of the $\text{ScN}_x\text{C}_{3-x}\text{@SACs}$ and $\text{ScN}_x\text{C}_{4-x}\text{@SACs}$ systems with three and four coordinations, respectively, decreased, and the structures were more stable, which is consistent with the phenomena of other systems studied by predecessors [56,57]. Figure 2 shows a close to negative correlation between the concentration of N atoms and formation energy, regardless of the structure of $\text{ScN}_x\text{C}_{3-x}\text{@SACs}$ and $\text{ScN}_x\text{C}_{4-x}\text{@SACs}$. Moreover, in the four-coordination $\text{ScN}_x\text{C}_{4-x}\text{@SACs}$ system, although the structures of the three kinds of ScN_2C_2 catalysts were different, their formation energies were similar, which is consistent with previous results [57]. However, Sc was not in the same horizontal plane as the underlying graphene in either optimized structures of $\text{ScN}_x\text{C}_{3-x}\text{@SACs}$ or $\text{ScN}_x\text{C}_{4-x}\text{@SACs}$. The reason for this is that the atomic radius of Sc is larger, and the Sc atom bulges on the surface, making some structures with less N atom doping concentration more unstable. However, the bulge of the Sc atom in the stable structure is more favorable for the adsorption of reactants. Because the incorporation of N atoms can alter the structure's electronegativity, the charge of C and N atoms coupled to Sc is higher, which results in the structures exhibiting increased levels of stability. Moreover, we demonstrated that the structures of ScN_3 with three coordinations and ScN_4 with four coordinations were more stable. Above all, different N/C coordination affected the stability of $\text{ScN}_x\text{C}_{3-x}\text{@SACs}$ and $\text{ScN}_x\text{C}_{4-x}\text{@SACs}$, with more N atoms resulting in a more stable structure.

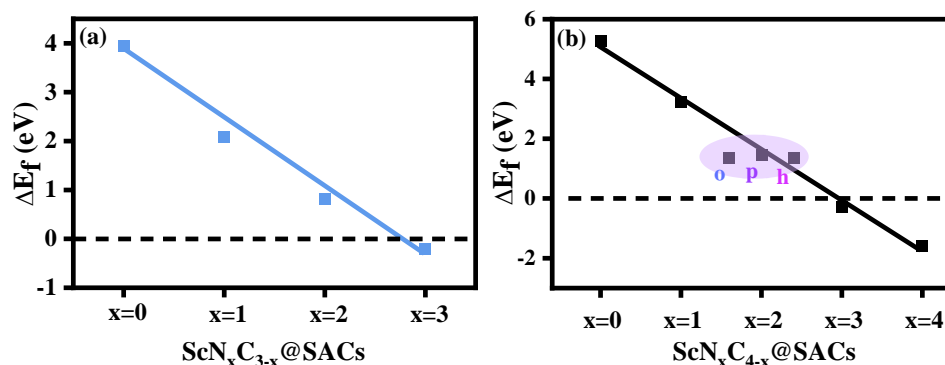


Figure 2. Formation energy (ΔE_f , eV) of the various structures of (a) $\text{ScN}_x\text{C}_{3-x}\text{@SACs}$ and (b) $\text{ScN}_x\text{C}_{4-x}\text{@SACs}$.

The partial densities of states (PDOS) of the $\text{ScN}_x\text{C}_{3-x}\text{@SACs}$ and $\text{ScN}_x\text{C}_{4-x}\text{@SACs}$ systems are shown in Figure 3. The analysis of Figure 3 shows that all the models passed through the Fermi level, indicating that all the structures had excellent conductivity. Furthermore, an effective overlap of the s, p, and d orbitals was observed, indicating that Sc formed bonds with the neighboring N and C atoms. In addition, the PDOS of the central part connected to Sc was studied. The overlap of the s, p, and d orbitals in the PDOS of the central part was more obvious, indicating that the Sc atom formed a bond with the base. The peak value of the d orbital rose with the increase of N atom doping concentration, which is similar to the law of formation energy in the $\text{ScN}_x\text{C}_{3-x}\text{@SACs}$ system. However, in the $\text{ScN}_x\text{C}_{4-x}\text{@SACs}$ system, although the peak value of the d orbital of ScN_3C was equivalent to three types of ScN_2C_2 structures, it still showed an overall upward trend.

Hence, different N/C coordination can significantly affect the electron distribution of the structure. The higher the concentration of N atoms is, the higher the peak value of the d orbital.

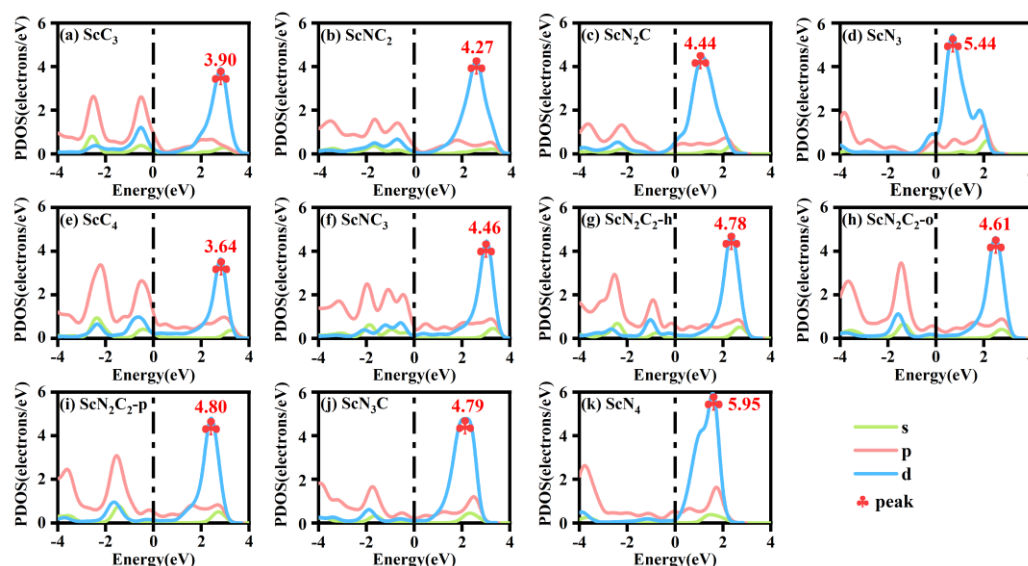


Figure 3. Partial densities of states (PDOS) of various structures of (a–d) $\text{ScN}_x\text{C}_{3-x}\text{@SACs}$ and (e–k) $\text{ScN}_x\text{C}_{4-x}\text{@SACs}$.

Based on Mulliken charge analysis, charge transfer occurred between the Sc, N, and C atoms. The electron transfer number is shown in Table S2, which indicates that the $\text{ScN}_x\text{C}_{3-x}\text{@SACs}$ and $\text{ScN}_x\text{C}_{4-x}\text{@SACs}$ structures formed chemical bonds, and the stability of the structure was explained from the side. In addition, different coordination structures followed the same law: with an increase in the N atom doping concentration, more electrons are lost by the Sc atom and gained by the N atoms, and the structure becomes more stable, which is consistent with the law of formation energy. Mulliken charge analysis for three-coordination ScN_3 and four-coordination ScN_4 with more stable and more negative values of the formation energy is further discussed, as shown in Figure 4. The charge distribution was symmetrical, corresponding to a symmetrical structure, which is consistent with the conclusion reached by other scholars on the charge distribution of symmetrical graphene-based materials [58,59]. The darker the color was, the more the charges on the structures gain or lose.

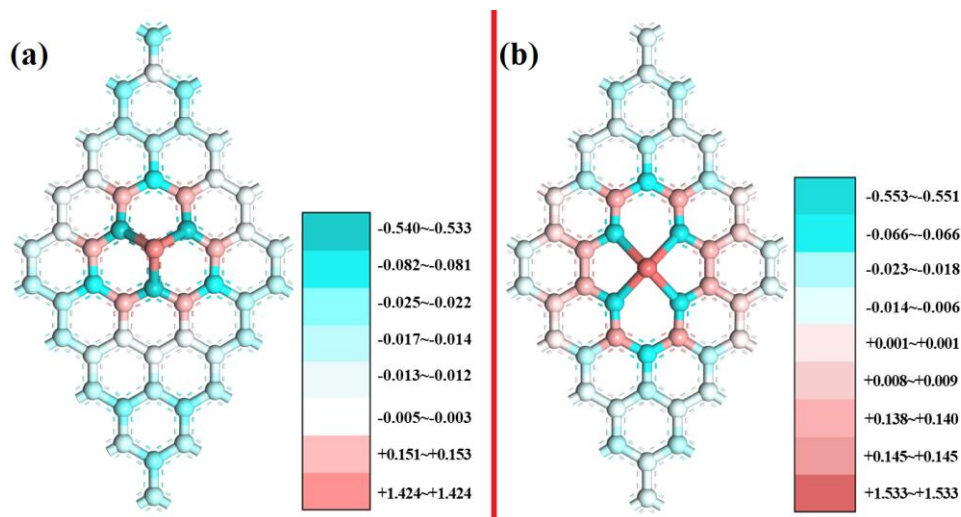


Figure 4. Mulliken charge analysis of (a) ScN_3 and (b) ScN_4 .

3.2. Adsorption Properties of the Intermediates

The adsorption capacity of the intermediates on the catalysts reflects their catalytic performance. Therefore, a series of adsorption configurations was obtained by constructing different intermediates and optimizing them in an alkaline environment. The adsorption of OH species was the first priority, and it indicated the availability of the reaction. In an alkaline environment, owing to the existence of a large amount of OH species and H₂O in the solution, the adsorption of OH species occurs as the first step in the OER. The detailed adsorption structures for different numbers of OH species and H₂O molecules are shown in Table S3. Therefore, calculation of the adsorption energy of ScN_xC_{3-x}@SACs and ScN_xC_{4-x}@SACs for OH species and H₂O and the comparison of adsorption capacity are prerequisites for subsequent work. As shown in Table S4, the value of the adsorption energy of different structures for OH species was greater than that for water, which also indicates that during the follow-up of the reaction process, H₂O can be desorbed in the structure to facilitate the reaction cycle. Moreover, with an increase in the concentration of doped N atoms, the adsorption capacity of the ScN_xC_{3-x}@SACs structures for OH species also increased. Although the rule of the ScN_xC_{4-x}@SACs system was not obvious, it still showed a similar general rule. Among them, N/C coordination in all N environments had the strongest adsorption capacity for OH species in ScN_xC_{3-x}@SACs and ScN_xC_{4-x}@SACs. The results are shown in Figure 5.

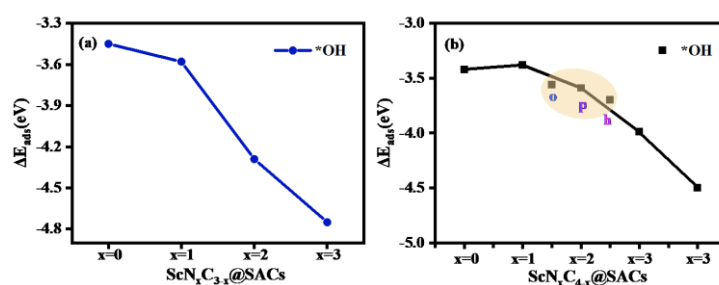


Figure 5. Adsorption energy (ΔE_{ads} , eV) of various (a) ScN_xC_{3-x}@SACs and (b) ScN_xC_{4-x}@SACs structures with adsorbed OH species.

However, based on the structures of the model, we found that the structures had a strong adsorption capacity for OH species. As the amount of OH species adsorption increased, some structures in addition to ScN₃ and ScN₄ in the ScN_xC_{3-x}@SACs and ScN_xC_{4-x}@SACs systems became increasingly unstable, as illustrated in Table S3. This structural instability resulted in structural deformation, which is not conducive to the study of the reaction and increases the experimental difficulty. However, after absorbing sufficient OH species, the structures of ScN₃ and ScN₄ could exist stably as Sc(OH)₂N₃ and Sc(OH)₂N₄. When the structure adsorbed enough OH species, further adsorption of OH species no longer occurred on the Sc atom, and they reacted with the ligand OH to generate intermediate products, as shown in Table S3. The detailed results are as follows: through structural optimization and DFT calculations, we found that three-coordination ScN₃ could adsorb up to three OH species, whereas four-coordination ScN₄ could adsorb up to four. When ScN₄ adsorbed a fifth OH species, it no longer adsorbed it on the Sc atom as a ligand but formed an OOH structure with a hydroxyl ligand and generated H₂O. While the ScN₃ structure with three coordination groups adsorbed a fourth OH species, it no longer adsorbed it on the Sc atom. As the number of adsorbed OH species increased, the adsorption capacity of both for OH species decreased, as shown in Figure 6. Hence, modification of the hydroxyl ligand weakened the adsorption strength of the structure to OH species.

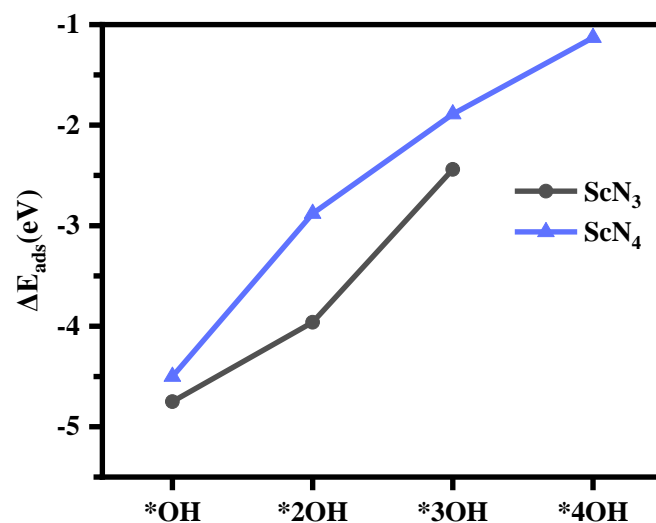


Figure 6. The adsorption energy (ΔE_{ads} , eV) of ScN₃ and ScN₄ with different numbers of OH species.

Therefore, ScN₃ and ScN₄ structures are two types of bases that can stably exist with two hydroxyl ligands modified in an alkaline environment and can be regarded as Sc(OH)₂N₃ and Sc(OH)₂N₄, respectively. A structural diagram of both is shown in Figure 7. Owing to the modification of the two hydroxyl ligands, the OH species adsorption capacity of the structure was reduced, which is beneficial for promoting the next reaction. Catalysts modified with hydroxyl ligand clusters displayed excellent OER performance [60,61]. Therefore, follow-up studies should be conducted.

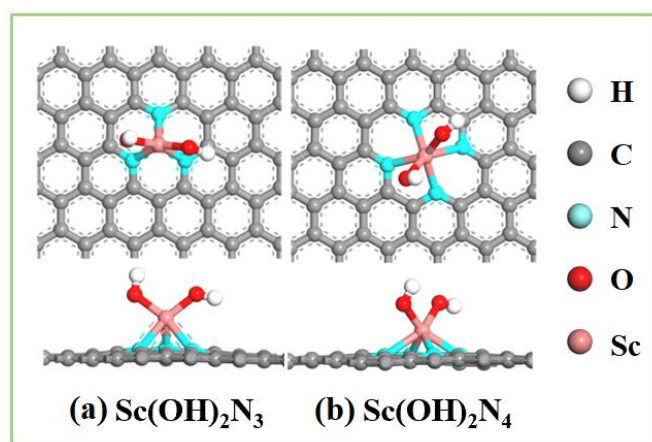


Figure 7. Diagram of the structures of (a) Sc(OH)₂N₃ and (b) Sc(OH)₂N₄.

The cyclicality of the OER is highly dependent on the desorption of the product O₂, and as the reverse process of adsorption, the degree of desorption is determined by the adsorption energy. The more positive the value of the adsorption energy is, the easier the product desorption. Next, the adsorption energies of O₂ on two bases with different numbers of OH ligands were calculated, and the adsorption configurations are listed in Table S5. Among them, the desorption of O₂ occurred in two forms: one was side-on (both oxygen atoms formed bonds with Sc atoms), and the other was end-on (only one oxygen atom formed a bond with the Sc atom). As shown in Figure 8, the ScN₃ and ScN₄ structures with double-hydroxyl ligands effectively desorbed O₂ so that the catalytic reaction was repeated. Moreover, both were more favorable for O₂ desorption with an increase in the number of hydroxyl ligands, and the value of the adsorption energy of O₂ adsorbed by Sc(OH)₂N₄ was positive, as shown in Table S6. In addition, an adsorption model of the intermediates was constructed, as shown in Table S7. It can be seen from the optimized structures (Table S7) that the adsorption configurations of Sc(OH)₂N₃ and Sc(OH)₂N₄

for O₂ all existed in end-on model. With the modification of two hydroxyl ligands, the adsorption capacity of the base for the next OH species was greater than that for water. The adsorption energies of Sc(OH)₂N₄ and Sc(OH)₂N₃ structures for intermediate products (OOH, O, and OH) are shown in Table S8. The values expressed that the intermediate products (OOH, O, and OH) could be effectively adsorbed on the base. The stability of Sc atoms with multiple adsorbates is shown in Table 1. This shows that the catalytic process of the formation of intermediate products (O, OH, and OOH) was stable, and the formation energy was negative.

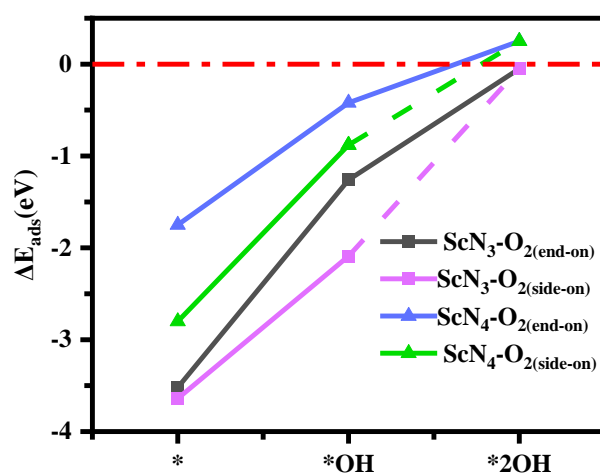


Figure 8. Adsorption energy (ΔE , eV) of ScN₃ and ScN₄ with different numbers of OH ligands for adsorbed O₂.

Table 1. Formation energy data (ΔE_f , eV) of reactive species on Sc(OH)₂N₃ and Sc(OH)₂N₄.

	ΔE_f^{*OH}	ΔE_f^{*O}	ΔE_f^{*OOH}	$\Delta E_f^{*O_2(endon)}$	$\Delta E_f^{*H_2O}$
Sc(OH) ₂ N ₃	-2.44	-2.98	-1.21	-0.05	-0.70
Sc(OH) ₂ N ₄	-1.89	-2.67	-0.94	0.25	-0.51

3.3. The Catalytic Activity of Sc(OH)₂N₃ and Sc(OH)₂N₄

To further investigate the catalytic performance of the Sc(OH)₂N₃ and Sc(OH)₂N₄ catalysts for the OER process, the Gibbs free energy change (ΔG) and overpotential (η) of each step of the reaction were calculated. First, $\Delta G_{*+OH \rightarrow *OH}$ and $\Delta G_{*OH+OH \rightarrow *2OH}$ were calculated, and the results are listed in Table S9. These values clearly indicated that ScN₃ and ScN₄ spontaneously generated Sc(OH)₂N₃ and Sc(OH)₂N₄, respectively, with two hydroxyl groups as ligands in an alkaline environment. It was further proven that ScN₃ and ScN₄ have a strong adsorption capacity for OH species. Figure 9 lists the ΔG and η of Sc(OH)₂N₃ and Sc(OH)₂N₄ catalysts for each step of reaction in the OER, and the detailed data are shown in Table S10. The potential determining step (PDS) of the reaction with Sc(OH)₂N₃ as the catalyst was $*OH + OH \rightarrow *O$, and the overpotential was 1.03 V. This could be related to the strong adsorption of OH species on the catalyst. Because of the strong adsorption of OH species, formation of $*O$ became more difficult, resulting in a higher overpotential. Two reaction paths were found when Sc(OH)₂N₄ was used as the catalyst. In the second step, there were two reaction pathways: $*OH + OH \rightarrow *O$ and $*OH + OH \rightarrow *2OH$. The first reaction path was the same as that of the Sc(OH)₂N₃ catalyst, and the second reaction path changed to $*2OH + OH \rightarrow *OOH$ in the third step. The potential determining step of both reaction paths was the second step: path 1: $*OH + OH \rightarrow *O$, path 2: $*OH + OH \rightarrow *2OH$. The overpotentials were 0.80 V and 1.10 V, respectively. Additionally, because the ΔG_2 of path 1 was 1.20 eV, which was 0.3 eV smaller than that of path 2, the reaction tended to proceed to the first reaction path when Sc(OH)₂N₄ was used as the catalyst. It can be concluded that

Sc(OH)₂N₄ with the reaction path *→*OH→*O→*O + *OH→*OOH + *OH→* is a suitable catalyst for the OER.

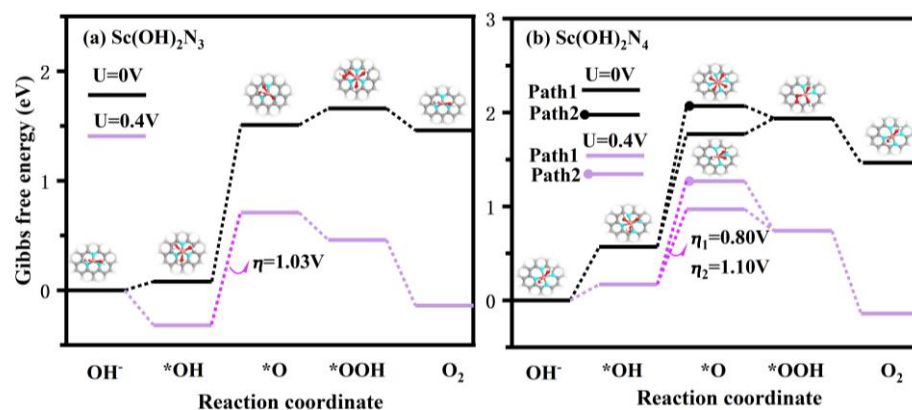


Figure 9. Possible reaction pathways of (a) Sc(OH)₂N₃ and (b) Sc(OH)₂N₄ structures. Pink atoms: Sc, gray atoms: C, blue atoms: N, red atoms: O, white atoms: H.

In addition, the possibility of producing H₂O₂ via side reactions was analyzed. For Sc(OH)₂N₃, the *OOH + OH→*O + H₂O₂ reaction ($\Delta G = 3.58$ eV) was endothermic and required more energy than the *OOH→*($\Delta G = -0.00$ eV) reaction, which was exothermic. For Sc(OH)₂N₄, the product of H₂O₂ was *OOH + OH→*O + H₂O₂ ($\Delta G = 3.56$ eV) and *2OH + OH→*OH + H₂O₂ ($\Delta G = 2.23$ eV), nor is it greater than the energy needed for *OOH→* ($\Delta G = -0.34$ eV) and *2OH + OH→*OOH ($\Delta G = 0.17$ eV). The specific ΔG values are listed in Table S11. Hence, the likelihood of side reactions forming H₂O₂ was very low. Therefore, Sc(OH)₂N₄ is a promising catalyst for the OER in alkaline environment.

3.4. The Origin of Catalytic Activity of Sc(OH)₂N₃ and Sc(OH)₂N₄

The PDOS of Sc(OH)₂N₃ and Sc(OH)₂N₄ and that of other atoms connected to Sc are shown in Figure 10. The two structures passed the Fermi level, proving the electrical conductivity of Sc(OH)₂N₃ and Sc(OH)₂N₄. In addition, by studying the PDOS of s, p, and d orbitals, it is found that there is a certain degree of overlap between p and d energies, indicating that the two hydroxyl ligands formed bonds with the Sc atoms. By comparing the PDOS in the central region of Sc(OH)₂N₃ and Sc(OH)₂N₄, the peak shape of the p orbital of Sc(OH)₂N₃ was found to be sharper than that of Sc(OH)₂N₄. This is because the coordination number of Sc(OH)₂N₄ and the number of doped N atoms are greater. The number of electrons obtained by the N atom was higher in the Sc(OH)₂N₄ structure, which is consistent with the structure obtained by Mulliken charge analysis, as shown in Figure S1.

Moreover, by comparing the PDOS of Sc(OH)₂N₃ and Sc(OH)₂N₄ with ScN₃ and ScN₄, we found that the number of electrons in the p orbital of the structure decreased with the modification of the two hydroxyl ligands, which can be obtained by comparing the area of the PDOS of the two structures. The peak deformation of the p orbital was sharper with the double-hydroxyl ligand modification. Second, the analysis of the PDOS comparison of Sc(OH)₂N₄ with ScN₄ and Sc(OH)₂N₃ with ScN₃ shows that the peaks of the 3d orbitals of Sc(OH)₂N₃ and Sc(OH)₂N₄ moved to the right, and the peak value dropped by almost three times. The structure without double-hydroxyl ligands had sharper 3d orbital peaks. This indicates that the presence of hydroxyl ligands can effectively change the properties of the structure and enhance its catalytic activity. In addition, a charge chromatic difference diagram was created by analyzing the Mulliken charges of Sc(OH)₂N₃ and Sc(OH)₂N₄, as shown in Figure S1. Compared with the results of Mulliken charge analysis of ScN₄ and ScN₃, the symmetry of the electron gain and loss distributions of Sc(OH)₂N₃ and Sc(OH)₂N₄ decreased under the modification of double-hydroxyl ligands. Compared with the Mulliken charge analysis structures of Sc(OH)₂N₃ and Sc(OH)₂N₄, the gain and loss charges of the main atoms were similar. Each N atom in the structure lost approximately

the same amount of charge, but the N atom in $\text{Sc}(\text{OH})_2\text{N}_4$ gained charge by a factor of three compared to the N atom in $\text{Sc}(\text{OH})_2\text{N}_3$. All these conclusions can be drawn from Table S12.

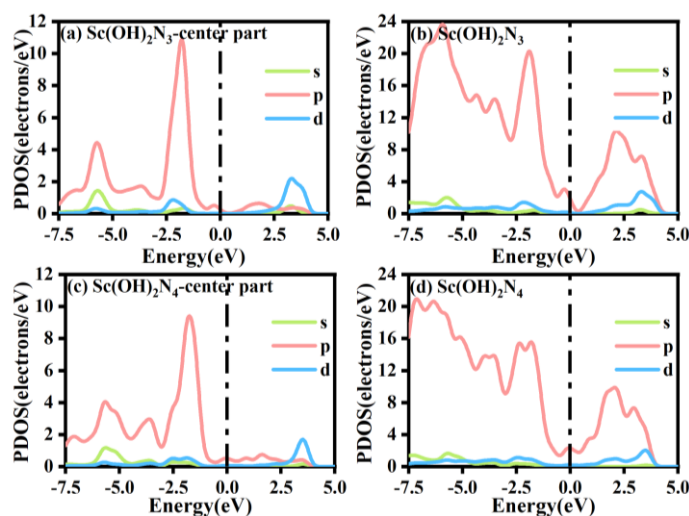


Figure 10. The PDOS of (a) $\text{Sc}(\text{OH})_2\text{N}_3$ -center part, (b) $\text{Sc}(\text{OH})_2\text{N}_3$, (c) $\text{Sc}(\text{OH})_2\text{N}_4$ -center part, and (d) $\text{Sc}(\text{OH})_2\text{N}_4$.

4. Conclusions

In this study, we explored the potential of Sc as an OER catalyst. Through DFT calculations, the structures of the $\text{ScN}_x\text{C}_{3-x}@SACs$ and $\text{ScN}_x\text{C}_{4-x}@SACs$ systems were optimized. We concluded that the structures of both the $\text{ScN}_x\text{C}_{3-x}@SACs$ and $\text{ScN}_x\text{C}_{4-x}@SACs$ systems were more stable with increasing N concentration. Hence, the concentration of N atoms can significantly affect the structural stability. In consideration of the N/C coordination in all N environments of $\text{ScN}_x\text{C}_{3-x}@SACs$ and $\text{ScN}_x\text{C}_{4-x}@SACs$ systems, ScN_3 and ScN_4 were the most stable structures. Moreover, the $\text{ScN}_x\text{C}_{3-x}@SACs$ and $\text{ScN}_x\text{C}_{4-x}@SACs$ systems exhibited a strong adsorption capacity for OH species in alkaline environments, and $\text{Sc}(\text{OH})_2\text{N}_3$ and $\text{Sc}(\text{OH})_2\text{N}_4$ structures with double-hydroxyl ligands could exist stably in alkaline environments. $\text{Sc}(\text{OH})_2\text{N}_3$ and $\text{Sc}(\text{OH})_2\text{N}_4$ could effectively desorb O_2 and H_2O to ensure a repeated catalytic sequence for the OER. The potential determining step (PDS) of $\text{Sc}(\text{OH})_2\text{N}_3$ was $^*\text{OH} + \text{OH} \rightarrow ^*\text{O}$, and its overpotential (η) was 1.03 V. $\text{Sc}(\text{OH})_2\text{N}_4$ had two reaction paths, and the potential determining steps of the two paths were as follows: path 1: $^*\text{OH} + \text{OH} \rightarrow ^*\text{O}$; path 2: $^*\text{OH} + \text{OH} \rightarrow ^*\text{2OH}$ ($\eta_1 = 0.80$ V; $\eta_2 = 1.10$ V). In conclusion, $\text{Sc}(\text{OH})_2\text{N}_4$ can be used as an effective catalyst for the OER because of its reasonable overpotential and structural stability. Meanwhile, PDOS and charge transfer analysis showed that double-hydroxyl ligands, as special modified ligands, could improve the catalytic activity of the reaction. Furthermore, different coordination structures affect catalytic activity. The method of preparing SACs based on metal–organic frameworks makes possible the experimental study of Sc@SACs. It is expected that our research will promote the development of rare earth catalysis.

Supplementary Materials: The following supporting information can be downloaded at: <https://www.mdpi.com/article/10.3390/batteries9030175/s1>.

Author Contributions: Conceptualization, Y.L., M.L., Y.H. and C.L.; methodology, Y.L., M.L. and Y.H.; software, Y.L., M.L. and Y.H.; validation, S.G.P. and C.L.; formal analysis, R.K.; investigation, Y.L.; resources, C.L.; data curation, Y.L.; writing—original draft preparation, Y.L.; writing—review and editing, C.L., R.K., T.-G.L. and S.G.P.; supervision, C.L. and S.G.P.; project administration, C.L. and S.G.P.; funding acquisition, C.L. and S.G.P. All authors have read and agreed to the published version of the manuscript.

Funding: This work was supported by the Natural Science Foundation of Jiangxi Province (Grant nos. 20212BAB203015 and 20212BCJL23053), the Research Foundation of the Education Department

of Jiangxi Province (Grant no. GJJ200808), and the Program of Qingjiang Excellent Young Talents (JXUSTQJYX2020002), Jiangxi University of Science and Technology. The authors also thank the National Research Foundation of Korea (NRF), funded by the Korean government, Ministry of Science, and ICT (MSIT) (No. 2021R1F1A1046648), Republic of Korea.

Data Availability Statement: Not applicable.

Conflicts of Interest: The authors declare that they have no known competing financial interests or personal relationships that could have influenced the work reported in this study.

References

1. Güney, T. Renewable energy consumption and sustainable development in high-income countries. *Int. J. Sustain. Dev. World Ecol.* **2021**, *28*, 376–385. [[CrossRef](#)]
2. Güney, T. Renewable energy, non-renewable energy and sustainable development. *Int. J. Sustain. Dev. World Ecol.* **2019**, *26*, 389–397. [[CrossRef](#)]
3. Hao, J.; Yuan, L.; Zhu, Y.; Jaroniec, M.; Qiao, S. Triple-Function Electrolyte Regulation toward Advanced Aqueous Zn-Ion Batteries. *Adv. Mater.* **2022**, *34*, 2206963. [[CrossRef](#)] [[PubMed](#)]
4. Iqbal, M.Z.; Rehman, A.-U.; Siddique, S. Prospects and challenges of graphene based fuel cells. *J. Energy Chem.* **2019**, *39*, 217–234. [[CrossRef](#)]
5. Zhang, J.; Xia, Z.; Dai, L. Carbon-based electrocatalysts for advanced energy conversion and storage. *Sci. Adv.* **2015**, *1*, e1500564. [[CrossRef](#)]
6. Wang, K.; Wang, X.; Li, Z.; Yang, B.; Ling, M.; Gao, X.; Lu, J.; Shi, Q.; Lei, L.; Wu, G.; et al. Designing 3d dual transition metal electrocatalysts for oxygen evolution reaction in alkaline electrolyte: Beyond oxides. *Nano Energy* **2020**, *77*, 105162. [[CrossRef](#)]
7. Dang, N.K.; Tiwari, J.N.; Sultan, S.; Meena, A.; Kim, K.S. Multi-site catalyst derived from Cr atoms-substituted CoFe nanoparticles for high-performance oxygen evolution activity. *Chem. Eng. J.* **2021**, *404*, 126513. [[CrossRef](#)]
8. Zheng, X.; Yang, J.; Xu, Z.; Wang, Q.; Wu, J.; Zhang, E.; Dou, S.; Sun, W.; Wang, D.; Li, Y. Ru–Co Pair Sites Catalyst Boosts the Energetics for the Oxygen Evolution Reaction. *Angew. Chem. Int. Ed.* **2022**, *61*, e202205946. [[CrossRef](#)]
9. An, L.; Wei, C.; Lu, M.; Liu, H.; Chen, Y.; Scherer, G.G.; Fisher, A.C.; Xi, P.; Xu, Z.J.; Yan, C.H. Recent Development of Oxygen Evolution Electrocatalysts in Acidic Environment. *Adv. Mater.* **2021**, *33*, e2006328. [[CrossRef](#)] [[PubMed](#)]
10. Yang, C.; Wu, Y.; Wang, Y.; Zhang, H.-N.; Zhu, L.-H.; Wang, X.-C. Electronic properties of double-atom catalysts for electrocatalytic oxygen evolution reaction in alkaline solution: A DFT study. *Nanoscale* **2022**, *14*, 187–195. [[CrossRef](#)] [[PubMed](#)]
11. Xu, D.; Long, X.; Xiao, J.; Zhang, Z.; Liu, G.; Tong, H.; Liu, Z.; Li, N.; Qian, D.; Li, J.; et al. Rationally constructing CoO and CoSe₂ hybrid with CNTs-graphene for impressively enhanced oxygen evolution and DFT calculations. *Chem. Eng. J.* **2021**, *422*, 129982. [[CrossRef](#)]
12. Charles, V.; Anumah, A.O.; Adegoke, K.A.; Adesina, M.O.; Ebuka, I.P.; Gaya, N.A.; Ogwuche, S.; Yakubu, M.O. Progress and challenges pertaining to the earthly-abundant electrocatalytic materials for oxygen evolution reaction. *Sustain. Mater. Technol.* **2021**, *28*, e00252. [[CrossRef](#)]
13. Ji, Y.; Dong, H.; Liu, C.; Li, Y. The progress of metal-free catalysts for the oxygen reduction reaction based on theoretical simulations. *J. Mater. Chem. A* **2018**, *6*, 13489–13508. [[CrossRef](#)]
14. Suen, N.-T.; Hung, S.-F.; Quan, Q.; Zhang, N.; Xu, Y.-J.; Chen, H.M. Electrocatalysis for the oxygen evolution reaction: Recent development and future perspectives. *Chem. Soc. Rev.* **2017**, *46*, 337–365. [[CrossRef](#)] [[PubMed](#)]
15. Wu, Z.; Lu, X.F.; Zang, S.; Lou, X.W. Non-Noble-Metal-Based Electrocatalysts toward the Oxygen Evolution Reaction. *Adv. Funct. Mater.* **2020**, *30*, 1910274. [[CrossRef](#)]
16. Sun, W.; Zhou, Z.; Zaman, W.Q.; Cao, L.-M.; Yang, J. Rational Manipulation of IrO₂ Lattice Strain on α -MnO₂ Nanorods as a Highly Efficient Water-Splitting Catalyst. *ACS Appl. Mater. Interfaces* **2017**, *9*, 41855–41862. [[CrossRef](#)] [[PubMed](#)]
17. Lee, Y.; Suntivich, J.; May, K.J.; Perry, E.E.; Shao-Horn, Y. Synthesis and Activities of Rutile IrO₂ and RuO₂ Nanoparticles for Oxygen Evolution in Acid and Alkaline Solutions. *J. Phys. Chem. Lett.* **2012**, *3*, 399–404. [[CrossRef](#)]
18. Chen, Y.; Rui, K.; Zhu, J.; Dou, S.X.; Sun, W. Recent Progress on Nickel-Based Oxide/(Oxy)Hydroxide Electrocatalysts for the Oxygen Evolution Reaction. *Chem. Eur. J.* **2019**, *25*, 703–713. [[CrossRef](#)]
19. Đurovič, M.; Hnát, J.; Bouzek, K. Electrocatalysts for the hydrogen evolution reaction in alkaline and neutral media. A comparative review. *J. Power Sources* **2021**, *493*, 229708. [[CrossRef](#)]
20. Wang, C.; Tong, H.; Lu, J.; Liu, B.; Zheng, F.; Tao, W.; Zhang, W.; Chen, Q. Boosting oxygen evolution reaction on graphene through engineering electronic structure. *Carbon* **2020**, *170*, 414–420. [[CrossRef](#)]
21. Sadeghi, S.; Amani, M. Co-doped triel–pnicogen graphene as metal-free catalyst for CO oxidation: Role of multi-center covalency. *J. Mol. Model.* **2019**, *25*, 77. [[CrossRef](#)]
22. Zhou, X.; Kang, L. A DFT study of graphene-FeN_x (x = 4, 3, 2, 1) catalysts for acetylene hydrochlorination. *Colloids Surfaces A Physicochem. Eng. Asp.* **2021**, *618*, 126495. [[CrossRef](#)]
23. Ede, S.R.; Luo, Z. Tuning the intrinsic catalytic activities of oxygen-evolution catalysts by doping: A comprehensive review. *J. Mater. Chem. A* **2021**, *9*, 20131–20163. [[CrossRef](#)]

24. Li, F.; Shu, H.; Liu, X.; Shi, Z.; Liang, P.; Chen, X. Electrocatalytic Activity and Design Principles of Heteroatom-Doped Graphene Catalysts for Oxygen-Reduction Reaction. *J. Phys. Chem. C* **2017**, *121*, 14434–14442. [[CrossRef](#)]
25. Bai, J.; Zhu, Q.; Lv, Z.; Dong, H.; Yu, J.; Dong, L. Nitrogen-doped graphene as catalysts and catalyst supports for oxygen reduction in both acidic and alkaline solutions. *Int. J. Hydrogen Energy* **2013**, *38*, 1413–1418. [[CrossRef](#)]
26. Wang, T.; Sang, X.; Zheng, W.; Yang, B.; Yao, S.; Lei, C.; Li, Z.; He, Q.; Lu, J.; Lei, L.; et al. Gas Diffusion Strategy for Inserting Atomic Iron Sites into Graphitized Carbon Supports for Unusually High-Efficient CO₂ Electroreduction and High-Performance Zn–CO₂ Batteries. *Adv. Mater.* **2020**, *32*, 2002430. [[CrossRef](#)]
27. Lee, W.H.; Ko, Y.-J.; Kim, J.-Y.; Min, B.K.; Hwang, Y.J.; Oh, H.-S. Single-atom catalysts for the oxygen evolution reaction: Recent developments and future perspectives. *Chem. Commun.* **2020**, *56*, 12687–12697. [[CrossRef](#)] [[PubMed](#)]
28. Shin, J.; Lee, Y.J.; Jan, A.; Choi, S.M.; Park, M.Y.; Choi, S.; Hwang, J.Y.; Hong, S.; Park, S.G.; Chang, H.J.; et al. Highly active and thermally stable single-atom catalysts for high-temperature electrochemical devices. *Energy Environ. Sci.* **2020**, *13*, 4903–4920. [[CrossRef](#)]
29. Kim, J.; Roh, C.-W.; Sahoo, S.K.; Yang, S.; Bae, J.; Han, J.W.; Lee, H. Highly Durable Platinum Single-Atom Alloy Catalyst for Electrochemical Reactions. *Adv. Energy Mater.* **2018**, *8*, 1701476. [[CrossRef](#)]
30. Zou, L.; Wei, Y.-S.; Hou, C.-C.; Li, C.; Xu, Q. Single-Atom Catalysts Derived from Metal–Organic Frameworks for Electrochemical Applications. *Small* **2021**, *17*, 2004809. [[CrossRef](#)] [[PubMed](#)]
31. Luo, Y.; Zhang, J.; Chen, J.; Chen, Y.; Zhang, C.; Luo, Y.; Wang, G.; Wang, R. Bi-functional electrocatalysis through synergetic coupling strategy of atomically dispersed Fe and Co active sites anchored on 3D nitrogen-doped carbon sheets for Zn-air battery. *J. Catal.* **2021**, *397*, 223–232. [[CrossRef](#)]
32. Kattel, S.; Wang, G. Reaction Pathway for Oxygen Reduction on FeN₄ Embedded Graphene. *J. Phys. Chem. Lett.* **2014**, *5*, 452–456. [[CrossRef](#)] [[PubMed](#)]
33. Kattel, S.; Wang, G. A density functional theory study of oxygen reduction reaction on Me–N₄ (Me = Fe, Co, or Ni) clusters between graphitic pores. *J. Mater. Chem. A* **2013**, *1*, 10790–10797. [[CrossRef](#)]
34. Ding, S.; Lyu, Z.; Sarnello, E.; Xu, M.; Fang, L.; Tian, H.; Karcher, S.E.; Li, T.; Pan, X.; McCloy, J.; et al. A MnO_x enhanced atomically dispersed iron–nitrogen–carbon catalyst for the oxygen reduction reaction. *J. Mater. Chem. A* **2022**, *10*, 5981–5989. [[CrossRef](#)]
35. Zhang, X.; Yang, Z.; Lu, Z.; Wang, W. Bifunctional CoN_x embedded graphene electrocatalysts for OER and ORR: A theoretical evaluation. *Carbon* **2018**, *130*, 112–119. [[CrossRef](#)]
36. Wang, R.; Lu, G.; Qiao, W.; Sun, Z.; Zhuang, H.; Yu, J. Catalytic effect of praseodymium oxide additive on the microstructure and electrical property of graphite anode. *Carbon* **2015**, *95*, 940–948. [[CrossRef](#)]
37. Kim, H.J.; Shin, D.; Jeong, H.; Jang, M.G.; Lee, H.; Han, J.W. Design of an Ultrastable and Highly Active Ceria Catalyst for CO Oxidation by Rare-Earth- and Transition-Metal Co-Doping. *ACS Catal.* **2020**, *10*, 14877–14886. [[CrossRef](#)]
38. Li, J.; Chu, B.; Xie, Z.; Deng, Y.; Zhou, Y.; Dong, L.; Li, B.; Chen, Z. Mechanism and DFT Study of Degradation of Organic Pollutants on Rare Earth Ions Doped TiO₂ Photocatalysts Prepared by Sol-Hydrothermal Synthesis. *Catal. Lett.* **2022**, *152*, 489–502. [[CrossRef](#)]
39. Chen, W.; Jiang, C.; Zhang, J.; Xu, J.; Xu, L.; Xu, X.; Li, J.; Cui, C. Rare-Earth-Catalyzed Selective 1,4-Hydrosilylation of Branched 1,3-Enynes Giving Tetrasubstituted Silyllallenes. *J. Am. Chem. Soc.* **2021**, *143*, 12913–12918. [[CrossRef](#)]
40. Abbott, D.F.; Pittkowski, R.K.; Macounova, K.; Nebel, R.; Marelli, E.; Fabbri, E.; Castelli, I.E.; Krtil, P.; Schmidt, T.J. Design and Synthesis of Ir/Ru Pyrochlore Catalysts for the Oxygen Evolution Reaction Based on Their Bulk Thermodynamic Properties. *ACS Appl. Mater. Interfaces* **2019**, *11*, 37748–37760. [[CrossRef](#)]
41. Zhu, M.; Zhao, C.; Liu, X.; Wang, X.; Zhou, F.; Wang, J.; Hu, Y.; Zhao, Y.; Yao, T.; Yang, L.-M.; et al. Single Atomic Cerium Sites with a High Coordination Number for Efficient Oxygen Reduction in Proton-Exchange Membrane Fuel Cells. *ACS Catal.* **2021**, *11*, 3923–3929. [[CrossRef](#)]
42. Zhao, J.; Liu, J.; Jin, C.; Wang, N.; Wang, F. Hexagonal La₂O₃ Nanocrystals Chemically Coupled with Nitrogen-Doped Porous Carbon as Efficient Catalysts for the Oxygen Reduction Reaction. *Chem. A Eur. J.* **2020**, *26*, 12606–12614. [[CrossRef](#)] [[PubMed](#)]
43. Murr, L.E. Summarizing Atom and Ion Structure: The Periodic Table of the Elements. In *Handbook of Materials Structures, Properties, Processing and Performance*; Springer International Publishing: Cham, Switzerland, 2015; pp. 83–95. [[CrossRef](#)]
44. Gismondi, P.; Kuzmin, A.; Unsworth, C.; Rangan, S.; Khalid, S.; Saha, D. Understanding the Adsorption of Rare-Earth Elements in Oligo-Grafted Mesoporous Carbon. *Langmuir* **2022**, *38*, 203–210. [[CrossRef](#)] [[PubMed](#)]
45. Wang, X.; Tang, Y.; Lee, J.-M.; Fu, G. Recent advances in rare-earth-based materials for electrocatalysis. *Chem Catal.* **2022**, *2*, 967–1008. [[CrossRef](#)]
46. Liu, J.; Kong, X.; Zheng, L.; Guo, X.; Liu, X.; Shui, J. Rare Earth Single-Atom Catalysts for Nitrogen and Carbon Dioxide Reduction. *ACS Nano* **2020**, *14*, 1093–1101. [[CrossRef](#)] [[PubMed](#)]
47. Lin, Z.-Z. Graphdiyne-supported single-atom Sc and Ti catalysts for high-efficient CO oxidation. *Carbon* **2016**, *108*, 343–350. [[CrossRef](#)]
48. Wang, Q.-Y.; Tong, Y.-C.; Yan, P.-J.; Xu, X.-J.; Li, Z. Attachment of CO to a (6, 6) CNT with a Sc adsorbate atom. *Struct. Chem.* **2019**, *30*, 399–408. [[CrossRef](#)]
49. Delley, B. From molecules to solids with the DMol3 approach. *J. Chem. Phys.* **2000**, *113*, 7756–7764. [[CrossRef](#)]
50. Perdew, J.P.; Burke, K.; Ernzerhof, M. Generalized gradient approximation made simple. *Phys. Rev. Lett.* **1996**, *77*, 3865–3868. [[CrossRef](#)]

51. Delley, B. Hardness conserving semilocal pseudopotentials. *Phys. Rev. B* **2002**, *66*, 155125. [[CrossRef](#)]
52. Delley, B. An all-electron numerical method for solving the local density functional for polyatomic molecules. *J. Chem. Phys.* **1990**, *92*, 508–517. [[CrossRef](#)]
53. Grimme, S. Semiempirical GGA-type density functional constructed with a long-range dispersion correction. *J. Comput. Chem.* **2006**, *27*, 1787–1799. [[CrossRef](#)]
54. Delley, B. The conductor-like screening model for polymers and surfaces. *Mol. Simul.* **2006**, *32*, 117–123. [[CrossRef](#)]
55. Yang, K.; Zaffran, J.; Yang, B. Fast prediction of oxygen reduction reaction activity on carbon nanotubes with a localized geometric descriptor. *Phys. Chem. Chem. Phys.* **2020**, *22*, 890–895. [[CrossRef](#)] [[PubMed](#)]
56. Liu, F.; Zhu, G.; Yang, D.; Jia, D.; Jin, F.; Wang, W. Systematic exploration of N, C configurational effects on the ORR performance of Fe–N doped graphene catalysts based on DFT calculations. *RSC Adv.* **2019**, *9*, 22656–22667. [[CrossRef](#)] [[PubMed](#)]
57. Liang, Z.; Luo, M.; Chen, M.; Qi, X.; Liu, J.; Liu, C.; Peera, S.G.; Liang, T. Exploring the oxygen electrode bi-functional activity of Ni–N–C-doped graphene systems with N, C co-ordination and OH ligand effects. *J. Mater. Chem. A* **2020**, *8*, 20453–20462. [[CrossRef](#)]
58. Revanappa, S.K.; Soni, I.; Siddalinganahalli, M.; Jayaprakash, G.K.; Flores-Moreno, R.; Nanjegowda, C.B. A Fukui Analysis of an Arginine-Modified Carbon Surface for the Electrochemical Sensing of Dopamine. *Materials* **2022**, *15*, 6337. [[CrossRef](#)]
59. Jayaprakash, G.K.; Swamy, B.E.K.; Flores-Moreno, R.; Pineda-Urbina, K. Theoretical and Cyclic Voltammetric Analysis of Asparagine and Glutamine Electrocatalytic Activities for Dopamine Sensing Applications. *Catalysts* **2023**, *13*, 100. [[CrossRef](#)]
60. Qin, R.; Zhou, L.; Liu, P.; Gong, Y.; Liu, K.; Xu, C.; Zhao, Y.; Gu, L.; Fu, G.; Zheng, N. Alkali ions secure hydrides for catalytic hydrogenation. *Nat. Catal.* **2020**, *3*, 703–709. [[CrossRef](#)]
61. Liang, Z.; Luo, M.; Chen, M.; Liu, C.; Peera, S.G.; Qi, X.; Liu, J.; Kumar, U.P.; Liang, T.L.T. Evaluating the catalytic activity of transition metal dimers for the oxygen reduction reaction. *J. Colloid Interface Sci.* **2020**, *568*, 54–62. [[CrossRef](#)] [[PubMed](#)]

Disclaimer/Publisher’s Note: The statements, opinions and data contained in all publications are solely those of the individual author(s) and contributor(s) and not of MDPI and/or the editor(s). MDPI and/or the editor(s) disclaim responsibility for any injury to people or property resulting from any ideas, methods, instructions or products referred to in the content.